Research Square

Preprints are preliminary reports that have not undergone peer review.
They should not be considered conclusive, used to inform clinical practice,
or referenced by the media as validated information.

hiPSC-derived small extracellular vesicles attenuate diabetic retinopathy with miR-30e-5p/NRIP1-mediated mitochondrial protection

Zhenggao Xie

zgxie87@163.com

Nanjing Drum Tower Hospital https://orcid.org/0000-0002-2587-157X

qian zhang

Department of Ophthalmology, Nanjing Drum Tower Hospital, Affiliated Hospital of Medical School, Nanjing University, Nanjing, China

yifei Tang

Department of Ophthalmology, Nanjing Drum Tower Hospital,Clinical College of Nanjing Medical University, Nanjing 210000, Jiangsu Province, China

Wenhao Guo

Department of Ophthalmology, Nanjing Drum Tower Hospital, Affiliated Hospital of Medical School, Nanjing University, Nanjing, China

Xiaoxue Zeng

Department of Ophthalmology, Nanjing Drum Tower Hospital, Affiliated Hospital of Medical School, Nanjing University, Nanjing, China

Chenchen Ma

Department of Ophthalmology, Nanjing Drum Tower Hospital, Affiliated Hospital of Medical School, Nanjing University, Nanjing, China

Ying Wei

Department of Ophthalmology, Nanjing Drum Tower Hospital, Affiliated Hospital of Medical School, Nanjing University, Nanjing, China

Article

Keywords: diabetic retinopathy, human induced pluripotent stem cells, small extracellular vesicles, miR-30e-5p, NRIP1, mitochondrial homeostasis

Posted Date: November 23rd, 2026

DOI: https://doi.org/10.21203/rs.3.rs-11566099/v1

License: This work is licensed under a Creative Commons Attribution 4.0 International License.
Read Full License

Additional Declarations: There is no conflict of interest

Abstract

Diabetic retinopathy (DR) is characterized by retinal microvascular dysfunction and breakdown of the blood-retinal barrier (BRB), with endothelial mitochondrial injury as an important contributor. We investigated whether human induced pluripotent stem cell-derived small extracellular vesicles (hiPSC-sEVs) reduce retinal vascular leakage and improve endothelial mitochondrial function in DR. In streptozotocin (STZ)-induced diabetic mice, intravitreal hiPSC-sEVs reduced retinal vascular leakage, partially restored tight-junction proteins, and alleviated mitochondrial oxidative stress. In human retinal microvascular endothelial cells exposed to high glucose, hiPSC-sEVs attenuated mitochondrial fragmentation and improved respiratory capacity. hiPSC-sEVs were enriched in miR-30e-5p, which directly targeted the NRIP1 3' UTR. Knockdown of miR-30e-5p in sEVs or overexpression of NRIP1 in recipient endothelial cells attenuated the protective effects of hiPSC-sEVs on mitochondria and barrier function. These results suggest that hiPSC-sEVs protect against DR by delivering miR-30e-5p to inhibit NRIP1 and restore mitochondrial homeostasis, supporting further development of hiPSC-sEVs as a therapeutic strategy for DR.

1. Introduction

DR is characterized by progressive injury to the retinal neurovascular unit, which includes endothelial cells, pericytes, glia, and neurons. Vascular leakage is a defining feature of this injury, and molecular profiling has linked disease risk to pathways beyond angiogenesis.[1, 2]Current treatments can reduce sight-threatening complications, but preventing anatomical progression does not necessarily preserve visual function. In Protocol W, preventive aflibercept was shown to reduce vision-threatening complications without enhancing four-year visual acuity. [3] Complementary approaches that protect retinal cells and maintain vascular integrity therefore remain important. Studies of cellular senescence have linked endothelial junctional disruption to retinal leakage in diabetic macular edema, supporting efforts to target the processes that drive barrier failure. [4]

Mitochondrial dysfunction is a potential link between prolonged diabetic exposure and endothelial injury. Endothelial-enriched specimens from proliferative DR exhibit mitochondrial dysfunction and reduced expression of oxidative phosphorylation-related programs. [5]Endothelial O-GlcNAcylation has also been linked to vascular dysfunction in DR. [6] Respiratory activity relies on both mitochondrial inner-membrane organization and the coordinated expression of nuclear and mitochondrial genes. [7, 8] Nuclear receptor-interacting protein 1 (NRIP1), which encodes receptor-interacting protein 140 (RIP140), is a potential regulatory node. RIP140 suppresses oxidative metabolism and antagonizes peroxisome proliferator-activated receptor-γ coactivator-1α (PGC-1α). [9, 10] RIP140 overexpression reduced mitochondrial ATP production and increased inflammatory signaling in ARPE-19 cells, and adenoviral RIP140 overexpression reduced electroretinogram a- and b-wave amplitudes in rat retina. [11] However, the role of NRIP1 in diabetic retinal endothelial mitochondria remains unclear, prompting an inquiry into NRIP1 alongside PGC-1α, nuclear respiratory factor 1 (NRF1), and mitochondrial transcription factor A (TFAM).

EVs harbor bioactive molecules and are being explored as therapeutic agents and delivery vehicles.[12, 13]hiPSCs provide an expandable source for such preparations. Vesicles derived from hiPSCs have facilitated diabetic wound repair, mitigated hyperoxia-associated lung injury, and conferred protection against acute kidney injury in experimental settings. [14–16] Recent findings have highlighted their anti-inflammatory properties in primary human macrophages and therapeutic effects of engineered hiPSC-sEVs in models of sinus node disease. [17–18] In the eye, hiPSC-derived EVs protected retinal ganglion cells in rat optic nerve crush models, and sEVs from hiPSC-derived neural progenitors did so in mouse optic nerve injury models. [19, 20] These findings support investigating hiPSC-sEVs in diabetic retinal vascular injury, where endothelial mitochondria are a key target. The RNA cargo of hiPSC-sEVs is a plausible source of this activity. These vesicles carry distinctive miRNA and circular RNA profiles [21], and the sequence features of miRNAs influence their vesicular release and cellular retention [22]. Presence in a preparation, however, does not establish delivery to recipient cells or engagement of a target [23, 24]. Nevertheless, which hiPSC-sEV cargo protects the diabetic retinal endothelium, and through which target, remains unresolved.

We examined whether hiPSC-sEVs reduce retinal vascular leakage in mice with STZ-induced diabetes and preserve mitochondrial function in hRMECs exposed to high glucose (HG). Given the role of RIP140 in suppressing oxidative metabolism and antagonizing PGC-1α [9–11], we selected NRIP1 as a candidate target before the miRNA screen. We assessed whether treatment reduced RIP140 abundance and increased PGC-1α, NRF1, and TFAM. Small-RNA sequencing and bioinformatic prediction were used to prioritize hiPSC-sEV miRNAs predicted to target NRIP1, and wild-type and binding-site-mutant reporters tested miR-30e-5p regulation of its 3' UTR. Functional experiments used hiPSC-sEVs with reduced miR-30e-5p abundance following lentiviral modification of donor hiPSCs. Separately, NRIP1 was overexpressed in recipient hRMECs to examine its influence on the treatment response.

2. Materials and methods

2.1. hiPSC culture and characterization

hiPSCs (Saibei Biotechnology, Beijing, China) were obtained at passage 14 and used through passage 30. Cells were maintained in mTeSR1 (STEMCELL Technologies, Vancouver, Canada) at 37°C and 5% CO2, passaged at approximately 90% confluence, and morphological examination was performed using inverted microscopy (Leica, Wetzlar, Germany). TRA-1-60 and SSEA4 were assessed via CytoFLEX S flow cytometry (Beckman Coulter, Brea, CA, USA), using unstained controls. Alkaline phosphatase activity was evaluated with a BCIP/NBT kit (Beyotime, Shanghai, China).

For immunofluorescence, cells were fixed with 4% paraformaldehyde for 15 min, permeabilized with 0.1% Triton X-100 for 15 min, and blocked with 2% BSA for 1 h. Primary antibodies against OCT4 (MA1-104, Invitrogen, Carlsbad, CA, USA) and NANOG (14295-1-AP, Proteintech, Wuhan, China) were applied at a dilution of 1:200 overnight at 4°C. After washing with PBS, secondary antibodies were incubated for 2 h at room temperature. Nuclei were counterstained with DAPI before imaging.

2.2. Lentiviral modification of hiPSCs

hiPSCs were transduced with the miR-30e-5p knockdown lentiviral vector LV-miR-30e-5p(−) or the control lentivirus LV-miR-NC (Corues Biotechnology, Nanjing, China), using the hU6-MCS-CBh-gcGFP-IRES-puromycin backbone according to the supplier's instructions. The provided miR-30e-5p-associated and control sequences were 5'-TGTAAACATCCTTGACTGGAAG-3' and 5'-TTCTCCGAACGTGTCACGT-3', respectively. The resulting preparations were designated sEV-miR-30e-5p-KD and sEV-miR-NC, with unmodified hiPSCs supplying standard sEVs. For isolated-sEV miRNA analysis, extracted RNA was normalized to equal concentrations prior to reverse transcription, and relative abundance was normalized to U6. Functional treatment doses were standardized by particle concentration.

2.3. sEV isolation and characterization

Complete mTeSR1 was precleared at 100,000 × g for 16 h. Each 80-mL conditioned medium sample underwent sequential centrifugation at 300 × g for 10 min, 2,000 × g for 10 min, and 10,000 × g for 30 min. Supernatants were centrifuged at 100,000 × g for 70 min using an Optima XE-100 and Type 90 Ti rotor (Beckman Coulter). Pellets were washed in pre-chilled PBS and subjected to another centrifugation at 100,000 × g for 70 min. Isolation was performed at 4°C. Final pellets were resuspended in 200 µL PBS and stored at − 80°C, minimizing freeze–thaw cycles.

Morphology was assessed via HT7800 transmission electron microscopy (Hitachi, Tokyo, Japan), and size and concentration measurements were conducted using ZetaView nanoparticle tracking analysis (Particle Metrix, Inning am Ammersee, Germany). CD63, CD81, TSG101, and calnexin levels were evaluated through Western blotting. Functional doses were standardized by particle number. [25]

2.4. DiD labeling and localization

sEVs were incubated with 5 µg/mL DiD (ab275319, Abcam, Cambridge, United Kingdom) for 30 min. Unincorporated dye was removed through ultracentrifugation at 100,000 × g for 70 min at 4°C, followed by resuspension in PBS. hRMECs were treated with labeled preparations for 24 h, then washed, fixed, counterstained with DAPI, and imaged using STELLARIS 5 confocal microscopy (Leica). Controls included untreated cells. In normal mice (n = 3), retinal sections and flat mounts were evaluated 14 days post-intravitreal administration, using IB4 labeling and PBS controls; no dye-only control was included.

2.5. Animal model and treatment

Male C57BL/6 mice (eight weeks, approximately 20 g; Cyagen Biosciences, Suzhou, China) were utilized under approval 2026AE01130 from Nanjing Drum Tower Hospital, adhering to the International Guiding Principles for Biomedical Research Involving Animals. STZ (55 mg/kg) was administered intraperitoneally for five consecutive days, and diabetes was defined by glucose levels exceeding 250 mg/dL three days post final injection. At 12 weeks, each eye received one intravitreal injection: 2 µL PBS in the Control and DM groups, or 1×10^9 sEV particles in 2 µL PBS in the DM + sEV group. Body weight

and glucose levels were monitored throughout the study. Four weeks later, cervical dislocation was performed under isoflurane anesthesia, and tissues were collected.

2.6. Histology and retinal vascular leakage

Eyes were fixed, dehydrated, paraffin-embedded, sectioned, and stained with hematoxylin and eosin for light microscopy analysis. Anesthetized mice received 2% Evans Blue via the tail vein at a dose of 30 mg/kg. After 1 hour, heparin-containing PBS was perfused until liver blanching was observed. Retinas were then separated from the RPE/choroid, and unfixed flat mounts were imaged using matched confocal settings. [26]

For quantification, weighed retinas were extracted in formamide at 60°C for 24 hours in the dark. After centrifugation, absorbance of the supernatant was measured at 620 nm against a concurrent standard curve, with results expressed as ng Evans Blue per mg of retinal wet weight, without plasma-dye normalization. Three independent left retinas were analyzed per group.

2.7. Immunofluorescence

Permeabilized and blocked retinal sections were incubated overnight at 4°C with primary antibodies against RIP140 (1:200; ab42126, Abcam,Cambridge, United Kingdom), PGC-1α (1:100; 66369-1-Ig, Proteintech), NRF1 (1:100; ab175932, Abcam), or TFAM (1:100; 22586-1-AP, Proteintech). Vascular structures were labeled with Alexa Fluor 594-conjugated IB4 (1:50; I32450, Invitrogen). After applying secondary antibodies for 1 hour at room temperature, DAPI-counterstained sections were imaged with matched STELLARIS 5 settings. Directly conjugated IB4 was visualized without secondary antibodies. Acquisition settings were consistent across treatment groups for each marker. ZO-1(1:100;61-7300,Invitrogen)immunofluorescence in hRMECs was assessed qualitatively, with DAPI counterstaining.

2.8. hRMEC culture and transduction

hRMECs (ScienCell, Carlsbad, CA, USA) were cultured in ECM (1001) supplemented with ECGS (1052) and 5% FBS at 37°C and 5% CO2. After 48 h of exposure to 30 mmol/L glucose, cells received 1 × 109 sEV particles/mL for an additional 24 hours under continuous HG exposure. Control cells were maintained in standard ECM.

Cells were transduced with an NRIP1-overexpressing lentivirus or its negative-control vector before HG exposure, and overexpression was confirmed by NRIP1 mRNA and RIP140 protein levels. Experimental groups included Control, HG, HG + sEV, HG + sEV-miR-30e-5p-KD, HG + sEV-miR-NC, HG + sEV + OE-NRIP1, and HG + sEV + OE-NC. OE-NRIP1 and OE-NC were also compared under normal culture conditions.

2.9. Mitochondrial membrane potential

Mitochondrial membrane potential was assessed by staining with JC-1 (C2003S, Beyotime) for 20 minutes at 37°C in darkness, followed by two washes with kit buffer and flow cytometric analysis. The red/green fluorescence ratio provided a measure of the mitochondrial membrane potential.

2.10. Mitochondrial network morphology

Live cells were labeled with Mito-Tracker Red CMXRos (C1035, Beyotime; 1:5000) for 20 minutes at 37°C in darkness. After replacing the medium with prewarmed conditions, cells were imaged using confocal microscopy, and mean branch length was measured using ImageJ Mitochondria Analyzer. [27]

2.11. Mitochondrial ultrastructure

hRMECs were fixed in 2.5% glutaraldehyde for 10 minutes at room temperature in darkness, then scraped in one direction and centrifuged at 200 × g for 5 minutes. The pellets were resuspended in fresh glutaraldehyde fixative, postfixed in 1% osmium tetroxide, dehydrated in acetone, and stained with 2% uranyl acetate. Ultrathin sections (approximately 70 nm) were examined using Hitachi transmission electron microscopy, assessing mitochondrial shape and cristae qualitatively.

2.12. Mitochondrial respiration

OCR was measured using the Seahorse XF Flex and the XF Cell Mito Stress Test Kit (103015-100, Agilent, Santa Clara, CA, USA). Cells reached approximately 80% confluence before analysis. Cartridges were hydrated overnight at 37°C without CO2. The assay medium was XF DMEM, pH 7.4 (103575-100), containing 10 mmol/L glucose, 1 mmol/L pyruvate, and 2 mmol/L glutamine. Cells were equilibrated for 45–60 minutes in the absence of CO2.

Sequential injections were performed with oligomycin (1.5 μmol/L), FCCP (1 μmol/L), and rotenone/antimycin A (0.5 μmol/L each). Basal and maximal respiration were corrected for non-mitochondrial OCR; ATP-coupled respiration was determined by the oligomycin-sensitive decrease. Data were analyzed using Wave software, normalized to BCA-measured protein, and reported as pmol/min/μg protein.

2.13. DNA extraction and relative mtDNA copy number

DNA was isolated from hRMECs or whole retinas using DC102-01 (Vazyme, Nanjing, China). SYBR Green qPCR measured mitochondrial targets relative to nuclear references: human CytB/ACTB and mouse Nd1/Hk2. Relative mtDNA abundance was expressed against the Control group, with primer sequences provided in Table 1.

2.14. RNA extraction and quantitative PCR

Retinal and cellular RNA was extracted using TRIzol. cDNA was generated with a first-strand synthesis kit (Vazyme), employing stem-loop reverse transcription for miR-30e-5p. Universal SYBR Master Mix (Vazyme) and StepOnePlus (Applied Biosystems, Foster City, CA, USA) were utilized for qPCR. NRIP1 mRNA and miRNA were normalized to GAPDH and U6, respectively. Relative expression was calculated using $2 - \Delta\Delta Ct$.[28, 29] ΔCt was defined as target Ct minus reference Ct, and $\Delta\Delta Ct$ represented the difference from the designated Control. Human NRIP1 primers corresponded to transcript NM_003489, with sequences listed in Table 1.

2.15. Oxidative stress-associated fluorescence

Retinal sections were stained with DHE (S0064S, Beyotime) for 30 minutes at 37°C, then mounted with antifade medium and imaged through confocal microscopy. ImageJ quantified red fluorescence relative to the Control. For cellular DCFH-DA staining, S0035S (Beyotime) was used as per the manufacturer's instructions, and flow cytometric mean fluorescence intensity was expressed relative to the Control. [30]

2.16. Small RNA sequencing and candidate selection

Three independent sEV preparations underwent sequencing by Shanghai Majorbio (Shanghai, China). QIAseq miRNA libraries (Qiagen, Hilden, Germany) were quantified using Qubit 4.0 (Thermo Fisher Scientific, Waltham, MA, USA), sequenced with NovaSeq X Plus (Illumina, San Diego, CA, USA), and analyzed via Majorbio Cloud. [31] After adapter and quality filtering, 18–32 nucleotide reads were aligned to the human reference genome. miRNAs were annotated against miRBase 22.0 and normalized as transcripts per million (TPM). Candidates were ranked by arithmetic mean TPM across the three preparations, with the Top20 subset displayed using log2(TPM + 1), without row-wise standardization. Candidate screening employed the Top100 set and ENCORI-derived miRanda and TargetScan lists of miRNAs predicted to regulate NRIP1, resulting in the identification of eight candidates. miR-30e-5p exhibited the highest mean TPM within this set and was selected for validation.

2.17. Dual-luciferase reporter assay

Wild-type and binding-site-mutant NRIP1 3'UTRs were cloned into pmirGLO and co-transfected into 293T cells with either a miR-30e-5p mimic or a negative control. Luciferase activity was measured after 48 hours using RG027 (Beyotime).

2.18. Western blotting

Cells and retinal tissues were lysed with RIPA buffer containing protease and phosphatase inhibitors (Beyotime, Shanghai, China). Protein concentration was determined by the BCA method. Equal amounts of protein (20 μg per sample) were separated by 10% SDS-PAGE and transferred onto polyvinylidene difluoride membranes (Millipore, Burlington, MA, USA). After blocking with 5% BSA in PBS for 1 h at room temperature, membranes were incubated overnight at 4°C with primary antibodies against RIP140 (1:1000; ab42126, Abcam), PGC-1α (1:1000; 66369-1-Ig, Proteintech), NRF1 (1:1000; ab175932, Abcam), TFAM (1:1000; 22586-1-AP, Proteintech), occludin (1:1000; ab216327, Abcam), or GAPDH (loading control). After washing, membranes were incubated with the corresponding secondary antibodies for 1 h at room temperature. Protein bands were visualized with Chemiluminescent Substrate kit.

2.19. Transendothelial electrical resistance

TEER was assessed in hRMEC monolayers following the indicated treatments using a Millicell ERS 3.0 digital voltohmmeter (MERS03000; Millipore, Burlington, MA, USA). The resistance of cell-free inserts was subtracted, and the corrected resistance was multiplied by the membrane area; results are expressed in Ω·cm².

2.20. Statistical analysis

Data were analyzed in GraphPad Prism 10 (GraphPad Software, Boston, MA, USA) and are presented as mean ± SD unless distribution plots are shown. Unless otherwise specified, at least three independent biological replicates were performed for all studies.Two-group comparisons used unpaired Student's t tests, and multiple groups were compared by one-way ANOVA with Tukey's test. $P < 0.05$ was considered significant. Group comparisons and significance notations are detailed in the figure legends. Sample sizes refer to independent animals or experimental runs; cells and fields within a run were treated as subsamples, not independent replicates.

Table 1

Target	Primer	Sequence 5'–3'
Human *CytB*	Forward	TCACCAGACCCTCAACCGC
Human *CytB*	Reverse	GCCTCCCCGATGTGTAGGA
Human *ACTB*	Forward	CTTTCCTGCCTGAGCTGACC
Human *ACTB*	Reverse	CCTAGAAGCATTTGCGTGG
Mouse *Nd1*	Forward	CTAGCAGAAACAAACCGGGC
Mouse *Nd1*	Reverse	CCGGCTGCGTATTCTACGTT
Mouse *Hk2*	Forward	GCCAGCCTCTCCTGATTTTAGTGT
Mouse *Hk2*	Reverse	GGGAACACAAAAGACCTCTTCTGG
Human *NRIP1*	Forward	CCGTTGTCATGTGCTGCAAG
Human *NRIP1*	Reverse	CGTGTTCTCGAGAATACTGCTGC
Mouse *Nrip1*	Forward	GAGGCCCGGAGAATCTGAAG
Mouse *Nrip1*	Reverse	TTTCGTTGCTCACCAAACGC
miR-30e-5p	Stem-loop RT	GTCGTATCCAGTGCAGGGTCCGAGGTATTCGCACTGGATACGACCTTCCA
miR-30e-5p	Forward	GCGCGTGTAAACATCCTTGAC
miRNA universal	Reverse	AGTGCAGGGTCCGAGGTATT
Human GAPDH	Forward	GGAGCGAGATCCCTCCAAAAT
Human GAPDH	Reverse	GGCTGTTGTCATACTTCTCATGG
Mouse GAPDH	Forward	CAGTGGCAAAGTGGAGATTG
Mouse GAPDH	Reverse	TGCCGTGAGTGGAGTCATAC

RT, reverse transcription. *ACTB* and *Hk2* were the human and mouse nuclear DNA references, respectively. *GAPDH* and U6 were the mRNA and miRNA expression references.

3. Results

3.1. Characterization of hiPSCs and hiPSC-derived sEVs

We first characterized the hiPSCs and hiPSC-sEVs. hiPSCs formed compact colonies and expressed OCT4 and NANOG, displaying positive alkaline phosphatase staining (Fig. 1A, B). Flow cytometry revealed TRA-1-60-positive and SSEA4-positive populations at 95.16% and 97.35%, respectively, with unstained cells defining the background (Fig. 1C). Differential ultracentrifugation yielded particles with vesicle-like morphology, rounded outlines, and a visible limiting membrane by transmission electron microscopy (Fig. 1D).

NTA showed a modal diameter of 92.6 nm and a median diameter of 97.9 nm for a representative hiPSC-sEV preparation (Fig. 1E). Western blotting confirmed the presence of CD63, CD81, and TSG101 in the isolated hiPSC-sEVs, while calnexin was detected in hiPSC lysates but absent in the sEV lane under the assay conditions (Fig. 1F). hRMECs were treated with DiD-labeled hiPSC-sEVs for 24 hours. DiD fluorescence appeared as discrete puncta near the nucleus and within the cell body, whereas untreated cells showed little signal (Fig. 1G). Together, these results support the identity and purity of the hiPSCs and hiPSC-sEV preparations.

3.2. hiPSC-sEV treatment attenuates retinal histological alterations and vascular leakage in diabetic mice

Treatment commenced after 12 weeks of STZ-induced diabetes, with retinas collected four weeks following a single intravitreal injection of 1 × 109 particles in 2 µL PBS per eye. H&E staining illustrated a well-defined laminar structure in Control retinas, characterized by closely arranged cells in the nuclear layers. DM retinas exhibited swollen nerve fiber layers and a looser cellular organization in the ganglion cell and inner nuclear layers. These alterations were less pronounced in DM + sEV sections, which demonstrated a more compact cellular arrangement (Fig. 2A).

In conjunction with histological changes, Evans Blue imaging revealed differences in retinal vascular leakage. Fluorescence in Control flat mounts was predominantly confined to the vascular network, whereas DM retinas exhibited diffuse fluorescence beyond the vascular pattern. DM + sEV retinas showed reduced extravascular fluorescence and more clearly delineated vessels (Fig. 2B). Quantitative analysis supported this observation. Retinal Evans Blue content, expressed as ng/mg retinal wet weight, was elevated in DM mice relative to Control and decreased following treatment, although the treated group remained above Control levels (Fig. 2C). Concurrently, retinal occludin abundance increased after hiPSC-sEV administration. Occludin levels were lower in DM compared to Control retinas, yet treatment resulted in increased abundance relative to DM, while still remaining below Control (Fig. 2D, E).

3.3. DiD-labeled hiPSC-sEVs show vascular-associated distribution in the retina

To examine retinal distribution following intravitreal administration, DiD tracing was conducted in normal mice. Retinal sections collected 14 days post-injection revealed DiD-associated fluorescence spatially associated with IB4-positive vascular structures (Fig. 2F). Retinal flat mounts displayed fluorescence along segments of the IB4-labeled vascular network, with enlarged views showing partial colocalization of DiD-labeled hiPSC-sEVs with retinal vessels, along with fluorescence located outside the vasculature (Fig. 2G).

3.4. hiPSC-sEV treatment improves retinal mitochondrial markers and reduces oxidative stress

In parallel with reduced retinal leakage, hiPSC-sEV treatment altered the abundance of mitochondrial regulatory proteins. DAPI demarcated the retinal nuclear bands, while IB4 characterized vascular profiles within the sections. Green protein-associated fluorescence extended into adjacent retinal tissue, not limited to the boxed vascular regions. DM retinal sections exhibited stronger RIP140 staining and weaker PGC-1α, NRF1, and TFAM staining compared to Control sections. Treatment resulted in decreased RIP140-associated fluorescence and increased signals for the other three proteins. Enlarged views illustrated their spatial relationship with IB4-positive structures (Fig. 3A). Whole-retina Western blotting corroborated these trends: RIP140 increased in DM mice and decreased following treatment, whereas PGC-1α, NRF1, and TFAM levels decreased with diabetes and increased in DM + sEV mice (Fig. 3B, C). Significant differences were observed for RIP140 and the other three proteins between DM and DM + sEV groups, with analyses conducted using three independent mice per group and one-way ANOVA with Tukey's multiple-comparison test. The protein levels approached Control values but did not completely return to baseline.

In addition to these protein changes, DHE-associated red fluorescence increased while the relative mtDNA copy number decreased in diabetic retinas. DHE images revealed red fluorescence within nuclear profiles, with more intense staining in DM sections. DHE fluorescence decreased after treatment but remained elevated compared to Control (Fig. 3D, E). The relative retinal mtDNA copy number, assessed using Nd1 and Hk2, increased in DM + sEV mice compared to DM while remaining lower than Control (Fig. 3F).

hiPSC-sEVs improve mitochondrial morphology and respiration in HG-exposed hRMECs

Building on the retinal findings, a literature-based challenge involving 30 mmol/L glucose for 48 hours was employed prior to hiPSC-sEV treatment in hRMECs. This treatment continued for 24 hours under HG conditions, allowing assessment of the cellular response during ongoing glucose exposure. MitoTracker imaging revealed elongated, interconnected tubules distributed throughout Control cells, whereas HG-exposed cells exhibited shorter, disconnected segments and more punctate profiles. Mean branch length

decreased under HG but increased following hiPSC-sEV treatment (Fig. 4A, B). Treated cells displayed longer connected segments, although their mean branch length remained lower than Control.

Alongside network remodeling, OCR curves distinguished basal respiration prior to oligomycin addition, with the oligomycin-sensitive component representing ATP-coupled respiration, and the FCCP-stimulated maximum. Oligomycin reduced OCR in all three groups, while FCCP produced a notable increase, and rotenone/antimycin A lowered the curves toward minimal residual levels. HG conditions decreased basal, maximal, and ATP-coupled respiration; all three parameters increased after hiPSC-sEV treatment (Fig. 4C, D). The treated curves fell between the Control and HG groups during both the basal and FCCP-stimulated phases, indicating partial respiratory recovery. Given the observed changes in RIP140 and mitochondrial indices, NRIP1 overexpression was evaluated separately under normal culture conditions. NRIP1 mRNA levels increased in comparison to both untransduced hRMECs and negative-control-transduced cells, with no significant difference between the two control groups (Fig. 4E). GFP-positive OE-NRIP1 cells displayed shorter branches and a more fragmented mitochondrial network than OE-NC cells (Fig. 4F, G). Basal, maximal, and ATP-coupled respiration were also diminished with NRIP1 overexpression (Fig. 4H, I).

3.5. hiPSC-sEV miRNA profiling identifies miR-30e-5p as a candidate regulator of NRIP1

We next profiled miRNAs in three independently isolated hiPSC-sEV samples by small-RNA sequencing. Among the 1,015 detected miRNA entries, pairwise Pearson correlations of untransformed TPM values ranged from 0.9715 to 0.9971 (Fig. 5A). The sequencing report annotated 13,313 genes in NR, 13,293 in Swiss-Prot, 12,727 in Pfam, 11,344 in KEGG, 13,155 in GO, and 13,267 in EggNOG (Fig. 5B); these counts reflect database coverage, not the number of miRNA targets. Target prediction yielded 14,820 unique genes. KEGG analysis mapped these targets to tight junctions, oxidative phosphorylation, mitophagy, and AMPK signaling pathways (Fig. 5C). GO analysis of predicted targets revealed genes involved in endothelial cell migration, proliferation, apoptosis regulation, and barrier formation (Fig. 5D). These annotations link predicted hiPSC-sEV miRNA targets to retinal endothelial junctions and mitochondrial homeostasis, providing context for candidate prioritization.

Within this miRNA profile, the top 20 miRNAs by mean TPM are displayed in Fig. 5E, with miR-30e-5p ranked 16th in the overall expression matrix. Because NRIP1 was selected before the miRNA screen, we used the Top100 miRNA set, which accounted for 96.63% of total mean TPM. Intersecting this set with ENCORI-derived miRanda and TargetScan predictions of miRNAs that target NRIP1 yielded eight candidates (Fig. 5F). Among these, miR-30e-5p exhibited the highest mean TPM across the three independent hiPSC-sEV samples, although its abundance varied between samples (Fig. 5G). Its predicted interaction with NRIP1 and comparatively high mean abundance further supported its selection for validation.

On this basis, we constructed wild-type and binding-site-mutant NRIP1 3' UTR reporters (Fig. 5H). In 293T cells, the miR-30e-5p mimic significantly reduced wild-type reporter activity compared to the

negative control, while the mutant reporter exhibited no substantial response (Fig. 5I). The mutation at the tested site abolished the reporter response, indicating sequence-specific regulation of the NRIP1 3' UTR by miR-30e-5p. Consistently, RT-qPCR showed reciprocal changes in miR-30e-5p abundance and NRIP1 mRNA expression in both models. In the retina, miR-30e-5p levels decreased in DM mice compared to Control and increased after hiPSC-sEV treatment (Fig. 5J). Conversely, retinal mRNA expression of the mouse gene Nrip1 rose with diabetes and fell following treatment (Fig. 5K). A similar pattern was observed in hRMECs, where HG decreased miR-30e-5p and increased NRIP1 mRNA, while hiPSC-sEV treatment elevated miR-30e-5p and reduced NRIP1 levels (Fig. 5L, M). All four measures moved toward Control values but did not fully return to baseline. miR-30e-5p was therefore prioritized for validation.

3.6. Vesicular miR-30e-5p depletion or NRIP1 overexpression attenuates hiPSC-sEV protection

To evaluate the impact of this regulatory interaction, hiPSCs were transduced with a miR-30e-5p knockdown lentiviral vector prior to sEV isolation. Concurrently, NRIP1 overexpression was assessed in recipient hRMECs. The hiPSC intervention was applied before isolating hiPSC-sEVs, while the recipient overexpression tested the response in cells receiving standard hiPSC-sEVs. Under sustained HG exposure, treatment with standard hiPSC-sEVs increased mean mitochondrial branch length, whereas the sEV-miR-30e-5p-KD and NRIP1-overexpression groups displayed shorter branches than HG + sEV cells (Fig. 6A). Representative electron micrographs depicted elongated mitochondrial profiles with recognizable cristae in Control cells, while HG conditions resulted in more rounded profiles with poorly defined internal structures. Standard hiPSC-sEV-treated cells exhibited better-preserved mitochondrial profiles and cristae than the two intervention groups (Fig. 6B), although these ultrastructural observations were qualitative.

In alignment with the structural findings, standard hiPSC-sEV treatment elevated the JC-1 red/green fluorescence ratio compared to HG and reduced DCF mean fluorescence intensity. Both intervention groups had lower JC-1 ratios and higher DCF fluorescence than HG + sEV cells (Fig. 6C, D). Changes in mitochondrial regulatory proteins paralleled these functional measurements. HG conditions increased RIP140 while decreasing PGC-1α, NRF1, and TFAM levels. Treatment with standard hiPSC-sEVs lowered RIP140 and increased the other three proteins. The sEV-miR-30e-5p-KD group exhibited higher RIP140 and lower levels of PGC-1α, NRF1, and TFAM compared to HG + sEV cells. NRIP1 overexpression also led to increased RIP140 and decreased PGC-1α, NRF1 and TFAM. (Fig. 6E, F).

In conjunction with these protein changes, standard hiPSC-sEV treatment led to increases in basal, maximal, and ATP-coupled respiration compared to HG. The three respiratory parameters were significantly lower in the sEV-miR-30e-5p-KD group than in HG + sEV cells, and the NRIP1-overexpression group also demonstrated lower respiratory values compared to HG + sEV (Fig. 6G, H). The curves displayed the most distinct separation during the FCCP-stimulated phase, with rotenone/antimycin A reducing OCR across all groups. Additionally, relative mtDNA copy number increased following standard

hiPSC-sEV treatment and was lower in the sEV-miR-30e-5p-KD group compared to HG + sEV cells (Fig. 6I).

Junctional protein and TEER measurements also showed differences in endothelial barrier recovery. ZO-1 staining decreased under HG and increased after standard hiPSC-sEV treatment. Representative images revealed weaker staining in the two intervention groups compared to HG + sEV cells (Fig. 6J). Occludin levels decreased under HG but increased after standard hiPSC-sEV treatment. Both intervention groups exhibited lower occludin levels than HG + sEV, and neither corresponding negative-control group significantly differed from HG + sEV (Fig. 6K, L). TEER assessed the electrical barrier integrity of hRMEC monolayers (Ω·cm²). TEER decreased under HG compared to Control and increased after standard hiPSC-sEV treatment. The sEV-miR-30e-5p-KD group and the NRIP1-overexpression group displayed lower TEER values compared to HG + sEV. Neither the sEV-miR-NC nor the OE-NC group showed significant differences from HG + sEV (Fig. 6M). Despite improvements, occludin and TEER values following standard treatment remained numerically below Control levels.

4. Discussion

hiPSC-sEV treatment attenuated retinal vascular leakage in diabetic mice and improved mitochondrial respiration and endothelial barrier function in HG-exposed hRMECs. These effects were observed after sustained diabetic exposure or established HG injury. Mice received a single intravitreal dose 12 weeks after STZ induction, and hRMECs were treated after 48 h of HG exposure, with HG maintained during the 24-h treatment. Thus, the effects were observed during continued metabolic challenge. Reduced retinal Evans blue accumulation and increased TEER provided complementary evidence of barrier protection in vivo and in vitro. Recovery of occludin and enhanced ZO-1 staining linked these functional changes to junctional preservation. A recent senolytic study links endothelial junctional disruption to retinal leakage in diabetic macular edema. [4] The lower TEER in the intervention groups mirrored the occludin changes.

The strongest mitochondrial evidence comes from combining structural and functional measurements. Longer branches and better-preserved mitochondrial profiles were associated with increases in basal, maximal, and ATP-coupled respiration. Higher JC-1 red/green ratios and lower DCF fluorescence provided additional measures of membrane potential and oxidative stress, respectively. The integrity of cristae architecture underpins oxidative phosphorylation, establishing a biological basis for linking ultrastructural observations to respiratory recovery. [7] Recovery of PGC-1α, NRF1, TFAM, and relative mtDNA abundance further supports improved mitochondrial maintenance. This interpretation aligns with the coordinated nuclear and mitochondrial gene expression necessary for respiratory complex assembly and function. [8] These findings do not resolve the rates of mitochondrial biogenesis, fusion, or fission and highlight that mitochondrial responses may differ across retinal compartments. Anderson and colleagues noted hyperfusion and impaired turnover in diabetic retinal neurodegeneration, [32]while the endothelial cells studied here exhibited shorter mitochondrial branches. Additionally, a shift from fatty acid oxidation to glycolysis has been shown to promote regenerative angiogenesis in experimental proliferative retinopathy. [33]

We prioritized NRIP1 before the miRNA screen because its protein, RIP140, suppresses oxidative metabolism and antagonizes PGC-1α activity.[9, 10] Retinal pigment epithelial studies have also linked RIP140 overexpression to diminished mitochondrial ATP production and inflammatory signaling. [11]Our normal-culture experiments extended this rationale to hRMECs, where NRIP1 overexpression resulted in shorter mitochondrial branches and reduced respiration. Under HG conditions, decreased RIP140 after hiPSC-sEV treatment coincided with recovery of PGC-1α, NRF1, and TFAM. miR-30e-5p was the most abundant of the eight predicted NRIP1 regulators. The reporter assay offered sequence-specific evidence, demonstrating that miR-30e-5p suppressed the wild-type NRIP1 3'UTR reporter while mutation of the tested site abolished this response. Reciprocal expression changes observed in retinas and hRMECs were consistent with this regulatory relationship. hiPSC-sEVs from knockdown hiPSCs produced weaker mitochondrial and barrier responses than standard hiPSC-sEVs. NRIP1 overexpression in recipient cells likewise reduced mitochondrial and barrier measures.

The broader hiPSC-EV literature supports both the therapeutic rationale and the significance of biological context. Protective effects have been documented in diabetic wound repair, hyperoxic lung injury, and acute kidney injury. [14–16] Ocular studies utilizing hiPSC-derived EVs or hiPSC-derived neural progenitor sEVs have demonstrated protection of retinal ganglion cells following optic nerve injury. [19, 20] The present findings build upon this research, addressing vascular leakage, endothelial respiration, and TEER. Profiling of non-coding RNAs and studies involving primary human macrophages have identified multiple candidate effectors within hiPSC-derived EVs, highlighting the need to consider additional cargo and recipient cell populations. [17, 21] Notably, Wang and colleagues reported that adipocyte-derived miR-30e-5p suppressed endothelial SLC7A11, reduced oxidative phosphorylation, and exacerbated atherosclerosis. [34]This divergent outcome highlights the importance of EV source, target availability, and disease context.

Several limitations constrain these findings. The use of male STZ-treated mice and HG-exposed hRMECs are restricted disease models, and biological replication was limited. The lack of an osmotic control prevents complete separation of glucose-specific effects from those related to osmolarity. Additionally, whole-retina measurements aggregate signals from multiple cell populations, complicating the attribution of the animal response solely to the endothelium. DHE and DCF fluorescence indicate oxidation-associated changes without pinpointing a specific oxidant or its mitochondrial source. [30]An identically processed unconditioned medium control was not included, leaving unresolved potential contributions from co-isolated medium components. [35, 36] MISEV2023 recommends such controls when interpreting EV-associated biological activity.[25]HiPSC lentiviral modification may also inadvertently alter cargo beyond the intended miRNA.

The next mechanistic priority is to connect endogenous target regulation with mitochondrial protection and barrier recovery. A miR-30e-5p-resistant NRIP1 rescue, evaluated alongside respiration and TEER with an appropriate vector control, would allow for specific testing of this relationship. AGO2 RNA immunoprecipitation could assess the association of miR-30e-5p and NRIP1 mRNA with silencing complexes, while perturbation of PGC-1α would help delineate downstream involvement. Future

development should focus on mitochondrial function and endothelial barrier integrity as complementary readouts for evaluating hiPSC-sEV activity. Linking these outcomes to cargo composition and target engagement would strengthen comparisons between production batches.[37, 38]This strategy aligns with EV drug-development recommendations that connect characterization, biological potency, and nonclinical evaluation. [39]The single-dose findings also warrant dose-ranging and longitudinal studies on retinal function and ocular safety. Establishing the duration of protection and whether reduced leakage correlates with preserved visual function would further clarify the therapeutic potential of hiPSC-sEVs in DR.

Overall, hiPSC-sEV treatment reduced diabetic retinal vascular leakage and enhanced mitochondrial morphology, respiration, and endothelial monolayer electrical barrier function under HG exposure. Candidate screening, NRIP1 3'UTR reporter assays, and lentiviral perturbation experiments support a role for miR-30e-5p/NRIP1 regulation in these responses.

Declarations

Conflict of interest

The authors declare no conflict of interest.

Funding

This work was supported by the National Natural Science Foundation of China (NSFC) (grant no. 82671392 to ZX), the Natural Science Foundation of Jiangsu Province (grant no. BK20251719 to ZX), and the 2024 Open Project for Integrative Chinese and Western Medicine Research of the Institute of Traditional Chinese Medicine, Nanjing University (grant no. ICMN2024003 to ZX).

Author Contributions

Qian Zhang: Conceptualization, Methodology, Resources, Project administration, Investigation, Formal analysis, Data curation, Writing - original draft. **Yifei Tang** : Investigation, Validation, Writing - review & editing. **Wenhao Guo**: Methodology, Resources, Data curation. **Xiaoxue Zeng**: Methodology, Resources,Formal analysis. **Chenchen Ma** : Methodology, Data curation. **Ying Wei**:Conceptualization, Resources, Methodology, Data curation, Writing - review & editing. **Zhenggao Xie**: Resources, Supervision, Validation, Writing - review & editing, Funding acquisition

Acknowledgements

We thank Shanghai Majorbio Bio-Pharm Technology Co., Ltd. (Shanghai, China) for providing miRNA sequencing services for this study.We thank Bullet Edits Limited for the linguistic editing and proofreading of the manuscript.

Data availability

The small-RNA sequencing data generated in this study have been deposited in the NCBI Gene Expression Omnibus (GEO) database under accession number GSE352703 (https://www.ncbi.nlm.nih.gov/geo/query/acc.cgi?acc=GSE352703).

References

1. Sivaprasad S, Wong TY, Gardner TW, Sun JK & Bressler NM. Diabetic retinal disease. *Nat Rev Dis Primers* 11, 62 (2025). https://doi.org/10.1038/s41572-025-00646-x
2. Yang S, Xin Z, Xiong R, Zhu Z, Li H, Chen Y, et al. Proteome atlas for mechanistic discovery and risk prediction of diabetic retinopathy. *Nat Commun* 16, 9636 (2025). https://doi.org/10.1038/s41467-025-64634-1
3. Maturi RK, Glassman AR, Josic K, Baker CW, Gerstenblith AT, Jampol LM, et al. Four-Year Visual Outcomes in the Protocol W Randomized Trial of Intravitreous Aflibercept for Prevention of Vision-Threatening Complications of Diabetic Retinopathy. *JAMA* 329, 376–385 (2023). https://doi.org/10.1001/jama.2022.25029
4. Crespo-Garcia S, Fournier F, Diaz-Marin R, Klier S, Ragusa D, Masaki L, et al. Therapeutic targeting of cellular senescence in diabetic macular edema: preclinical and phase 1 trial results. *Nat Med* 30, 443–454 (2024). https://doi.org/10.1038/s41591-024-02802-4
5. McCann MA, Baccouche B, Li Y, Roy P, Sheth N, Lim JI, et al. Proliferative diabetic retinopathy subtypes defined by immune defense and endothelial mitochondrial dysfunction. *Signal Transduct Target Ther* 10, 350 (2025). https://doi.org/10.1038/s41392-025-02448-9
6. Lei Y, Liu Q, Chen B, Wu F, Li Y, Dong X, et al. Protein O-GlcNAcylation coupled to Hippo signaling drives vascular dysfunction in diabetic retinopathy. *Nat Commun* 15, 9334 (2024). https://doi.org/10.1038/s41467-024-53601-x
7. Daumke O & van der Laan M. Molecular machineries shaping the mitochondrial inner membrane. *Nat Rev Mol Cell Biol* 26, 706–724 (2025). https://doi.org/10.1038/s41580-025-00854-z
8. Liu YJ, Sulc J & Auwerx J. Mitochondrial genetics, signalling and stress responses. *Nat Cell Biol* 27, 393–407 (2025). https://doi.org/10.1038/s41556-025-01625-w
9. Powelka AM, Seth A, Virbasius JV, Kiskinis E, Nicoloro SM, Guilherme A, et al. Suppression of oxidative metabolism and mitochondrial biogenesis by the transcriptional corepressor RIP140 in mouse adipocytes. *J Clin Invest* 116, 125–136 (2006). https://doi.org/10.1172/jci26040

10. Hallberg M, Morganstein DL, Kiskinis E, Shah K, Kralli A, Dilworth SM, et al. A functional interaction between RIP140 and PGC-1alpha regulates the expression of the lipid droplet protein CIDEA. *Mol Cell Biol* 28, 6785–6795 (2008). https://doi.org/10.1128/mcb.00504-08
11. Guo Z, Shen Y, Zhong J, Li Z, Guo Q, Yao X, et al. RIP140-Mediated NF-κB Inflammatory Pathway Promotes Metabolic Dysregulation in Retinal Pigment Epithelium Cells. *Curr Issues Mol Biol* 44, 5788–5801 (2022). https://doi.org/10.3390/cimb44110393
12. Kumar MA, Baba SK, Sadida HQ, Marzooqi SA, Jerobin J, Altemani FH, et al. Extracellular vesicles as tools and targets in therapy for diseases. *Signal Transduct Target Ther* 9, 27 (2024). https://doi.org/10.1038/s41392-024-01735-1
13. Di Ianni E, Obuchi W, Breyne K & Breakefield XO. Extracellular vesicles for the delivery of gene therapy. *Nat Rev Bioeng* 3, 360–373 (2025). https://doi.org/10.1038/s44222-025-00277-7
14. Levy D, Abadchi SN, Shababi N, Ravari MR, Pirolli NH, Bergeron C, et al. Induced Pluripotent Stem Cell-Derived Extracellular Vesicles Promote Wound Repair in a Diabetic Mouse Model via an Anti-Inflammatory Immunomodulatory Mechanism. *Adv Healthc Mater* 12, e2300879 (2023). https://doi.org/10.1002/adhm.202300879
15. Saneh H, Wanczyk H, Walker J & Finck C. Effectiveness of extracellular vesicles derived from hiPSCs in repairing hyperoxia-induced injury in a fetal murine lung explant model. *Stem Cell Res Ther* 15, 80 (2024). https://doi.org/10.1186/s13287-024-03687-3
16. Collino F, Lopes JA, Tapparo M, Tortelote GG, Kasai-Brunswick TH, Lopes GMC, et al. Extracellular Vesicles Derived from Induced Pluripotent Stem Cells Promote Renoprotection in Acute Kidney Injury Model. *Cells* 9, 453 (2020). https://doi.org/10.3390/cells9020453
17. Fitzsimons S, Oggero S, Egan BP, Dillon ET, Martín MM, Clerkin S, et al. Extracellular vesicles derived from induced pluripotent stem cells mediate anti-inflammatory effects in primary human macrophages. *Sci Rep* 16, 21287 (2026). https://doi.org/10.1038/s41598-026-49621-w
18. Liu H, Zeng Y, Fan W, Lan X, Liu C, He Y, et al. Platelet-bioengineered hiPSC-sEVs achieve targeted repair of fibrotic sinoatrial node in preclinical SND models. *Nat Commun* 16, 10974 (2025). https://doi.org/10.1038/s41467-025-65936-0
19. Lu Y, Guo M, Liu Y, Liu H, Liao M, He K, et al. Human induced pluripotent stem cell-derived extracellular vesicles promote neuroprotection effects in rat optic nerve crush model. *Exp Eye Res* 258, 110505 (2025). https://doi.org/10.1016/j.exer.2025.110505
20. Li T, Xing HM, Qian HD, Gao Q, Xu SL, Ma H, et al. Small extracellular vesicles derived from human induced pluripotent stem cell-differentiated neural progenitor cells mitigate retinal ganglion cell degeneration in a mouse model of optic nerve injury. *Neural Regen Res* 20, 587–597 (2025). https://doi.org/10.4103/NRR.NRR-D-23-01414
21. Barilani M, Peli V, Manzini P, Pistoni C, Rusconi F, Pinatel EM, et al. Extracellular Vesicles from Human Induced Pluripotent Stem Cells Exhibit a Unique MicroRNA and CircRNA Signature. *Int J Biol Sci* 20, 6255–6278 (2024). https://doi.org/10.7150/ijbs.100113

22. Garcia-Martin R, Wang G, Brandão BB, Zanotto TM, Shah S, Kumar Patel S, et al. MicroRNA sequence codes for small extracellular vesicle release and cellular retention. *Nature* 601, 446–451 (2022). https://doi.org/10.1038/s41586-021-04234-3
23. Albanese M, Chen YA, Hüls C, Gärtner K, Tagawa T, Mejias-Perez E, et al. MicroRNAs are minor constituents of extracellular vesicles that are rarely delivered to target cells. *PLoS Genet* 17, e1009951 (2021). https://doi.org/10.1371/journal.pgen.1009951
24. Ripoll L, Zickler AM, Vader P, El Andaloussi S, Verweij FJ & van Niel G. Biology and therapeutic potential of extracellular vesicle targeting and uptake. *Nat Rev Mol Cell Biol* 27, 358–376 (2026). https://doi.org/10.1038/s41580-025-00922-4
25. Welsh JA, Goberdhan DCI, O'Driscoll L, Buzas EI, Blenkiron C, Bussolati B, et al. Minimal information for studies of extracellular vesicles (MISEV2023): From basic to advanced approaches. *J Extracell Vesicles* 13, e12404 (2024). https://doi.org/10.1002/jev2.12404
26. Qaum T, Xu Q, Joussen AM, Clemens MW, Qin W, Miyamoto K, et al. VEGF-initiated blood-retinal barrier breakdown in early diabetes. *Invest Ophthalmol Vis Sci* 42, 2408–2413 (2001). https://pubmed.ncbi.nlm.nih.gov/11527957/
27. Chaudhry A, Shi R & Luciani DS. A pipeline for multidimensional confocal analysis of mitochondrial morphology, function, and dynamics in pancreatic β-cells. *Am J Physiol Endocrinol Metab* 318, E87-E101 (2020). https://doi.org/10.1152/ajpendo.00457.2019
28. Livak KJ & Schmittgen TD. Analysis of relative gene expression data using real-time quantitative PCR and the 2(-Delta Delta C(T)) Method. *Methods* 25, 402–408 (2001). https://doi.org/10.1006/meth.2001.1262
29. Bustin SA, Ruijter JM, van den Hoff MJB, Kubista M, Pfaffl MW, Shipley GL, et al. MIQE 2.0: Revision of the Minimum Information for Publication of Quantitative Real-Time PCR Experiments Guidelines. *Clin Chem* 71, 634–651 (2025). https://doi.org/10.1093/clinchem/hvaf043
30. Murphy MP, Bayir H, Belousov V, Chang CJ, Davies KJA, Davies MJ, et al. Guidelines for measuring reactive oxygen species and oxidative damage in cells and in vivo. *Nat Metab* 4, 651–662 (2022). https://doi.org/10.1038/s42255-022-00591-z
31. Ren Y, Yu G, Shi C, Liu L, Guo Q, Han C, et al. Majorbio Cloud: A one-stop, comprehensive bioinformatic platform for multiomics analyses. *iMeta* 1, e12 (2022). https://doi.org/10.1002/imt2.12
32. Anderson A, Alfahad N, Wimalachandra D, Bouzinab K, Rudzinska P, Wood H, et al. Relaxation of mitochondrial hyperfusion in the diabetic retina via N6-furfuryladenosine confers neuroprotection regardless of glycaemic status. *Nat Commun* 15, 1124 (2024). https://doi.org/10.1038/s41467-024-45387-9
33. Cagnone G, Pundir S, Betus C, Agnihotri T, Ren A, -Kim JS, et al. Metabolic reprogramming of the neovascular niche promotes regenerative angiogenesis in proliferative retinopathy. *Nat Commun* 16, 5377 (2025). https://doi.org/10.1038/s41467-025-60061-4

34. Wang C, She J, Qian X, Wu H, Hao W, Liang X, et al. Obesity Increases Atherosclerosis Susceptibility via an Intertissue miR-30e-SLC7A11 Axis. *Circ Res* 139, e328493 (2026). https://doi.org/10.1161/CIRCRESAHA.126.328493
35. Morales-Sanfrutos J, Etxeberria-Ugartemendia J, Barroso-Gomila O, González E, Sendino M, Ximénez-Embún P, et al. Defining the reference proteomes for small extracellular vesicles and non-vesicular components. *Nat Cell Biol* 28, 622–639 (2026). https://doi.org/10.1038/s41556-026-01878-z
36. Zhang Q, Jeppesen DK, Higginbotham JN, Franklin JL & Coffey RJ. Comprehensive isolation of extracellular vesicles and nanoparticles. *Nat Protoc* 18, 1462–1487 (2023). https://doi.org/10.1038/s41596-023-00811-0
37. Cheng L & Hill AF. Therapeutically harnessing extracellular vesicles. *Nat Rev Drug Discov* 21, 379–399 (2022). https://doi.org/10.1038/s41573-022-00410-w
38. Chaudhari AP, Budayr OM, Bonacquisti EE, Kussatz CC, Bannon MS, Law KJ, et al. The Status of Extracellular Vesicles as Drug Carriers and Therapeutics. *Nat Rev Bioeng* 4, 301–318 (2026). https://doi.org/10.1038/s44222-026-00405-x
39. Xu G, Jin J, Fu Z, Wang G, Lei X, Xu J, et al. Extracellular vesicle-based drug overview: research landscape, quality control and nonclinical evaluation strategies. *Signal Transduct Target Ther* 10, 255 (2025). https://doi.org/10.1038/s41392-025-02312-w

Graphical Abstract

Graphical Abstract is not available with this version.

Working model of hiPSC-sEV-associated mitochondrial and retinal vascular protection.

This schematic summarizes the preparation of hiPSC-sEVs and the proposed mechanism by which hiPSC-sEVs protect the retinal endothelium under diabetic stress. hiPSC-sEVs are isolated from hiPSC-conditioned medium by differential centrifugation followed by ultracentrifugation; these vesicles are positive for CD63, CD81, and TSG101 and carry miR-30e-5p. Intravitreal delivery of hiPSC-sEVs alleviates retinal barrier breakdown in STZ-induced diabetic mice. In high-glucose-challenged hRMECs, hiPSC-sEV-derived miR-30e-5p is proposed to suppress NRIP1/RIP140 expression. Reduced NRIP1/RIP140 is associated with elevated PGC-1α, NRF1, and TFAM levels, which together contribute to mitochondrial protection—manifest as improved respiratory function and reduced oxidative stress—and are accompanied by preservation of endothelial tight junctions (partial recovery of occludin and ZO-1, and increased TEER). Knockdown of miR-30e-5p in sEVs or overexpression of NRIP1 in recipient hRMECs attenuates these protective effects on mitochondria and endothelial barriers.

Figures

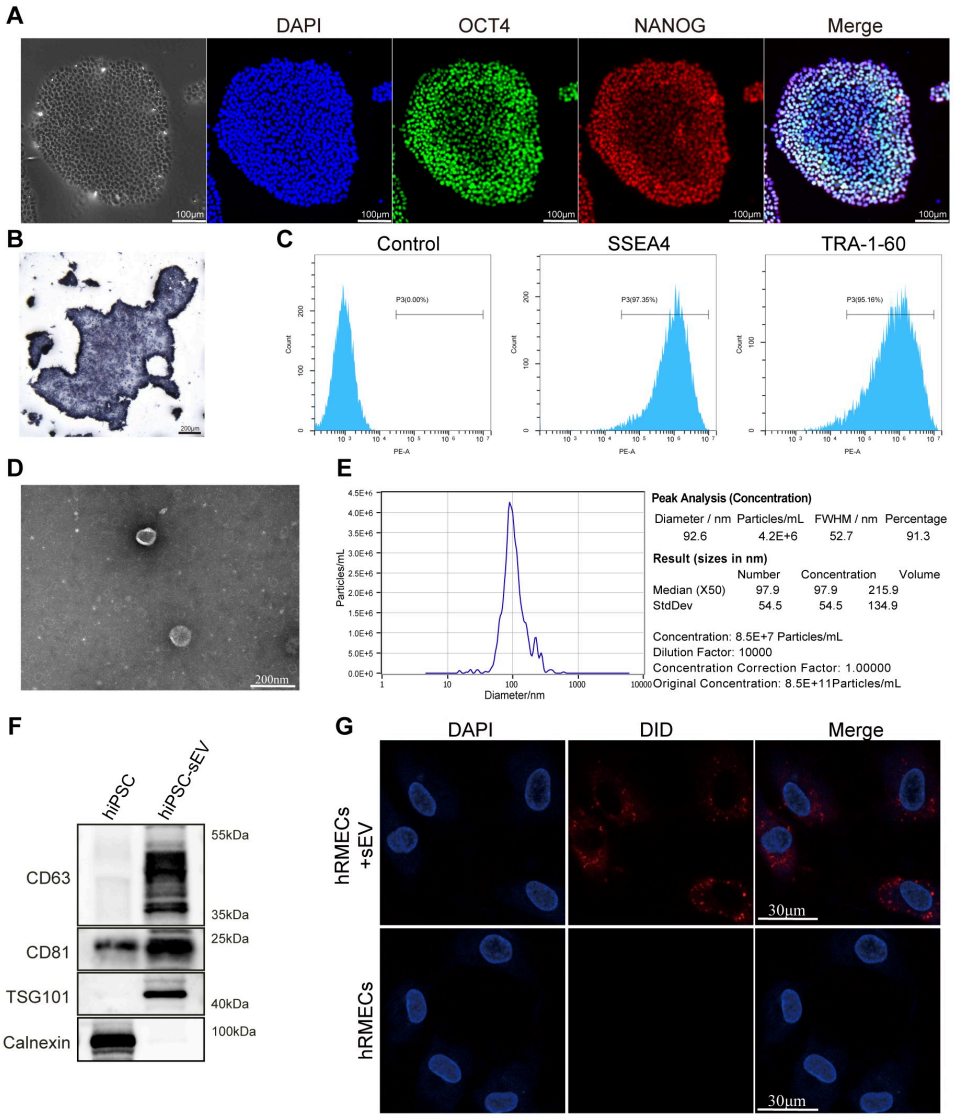

Figure 1

Characterization of hiPSCs and hiPSC-sEV preparations

(A) Immunofluorescence staining of OCT4 and NANOG in hiPSC colonies, with nuclear counterstaining. Scale bars, 100 μm. (B) Alkaline phosphatase staining of hiPSC colonies. Scale bar, 200 μm. (C) Flow cytometric analysis of TRA-1-60 and SSEA4. Unstained cells served as controls; the corresponding

positive populations were 95.16% and 97.35%, respectively. (D) Representative transmission electron microscopy image of the hiPSC-sEV preparation. Scale bar, 200 nm. (E) Nanoparticle tracking analysis of particle size distribution. Particle size and concentration were measured in preparations from three independent culture and isolation batches. (F) Western blot detection of CD63, CD81, TSG101, and calnexin in hiPSC lysates and sEV preparations; (G) Confocal images of untreated hRMECs and hRMECs incubated with DiD-labeled preparations for 24 h. DiD-associated fluorescence is red, and DAPI-stained nuclei are blue. Scale bars, 30 μm. hiPSC, human induced pluripotent stem cell; sEV, small extracellular vesicle; hRMEC, human retinal microvascular endothelial cell.

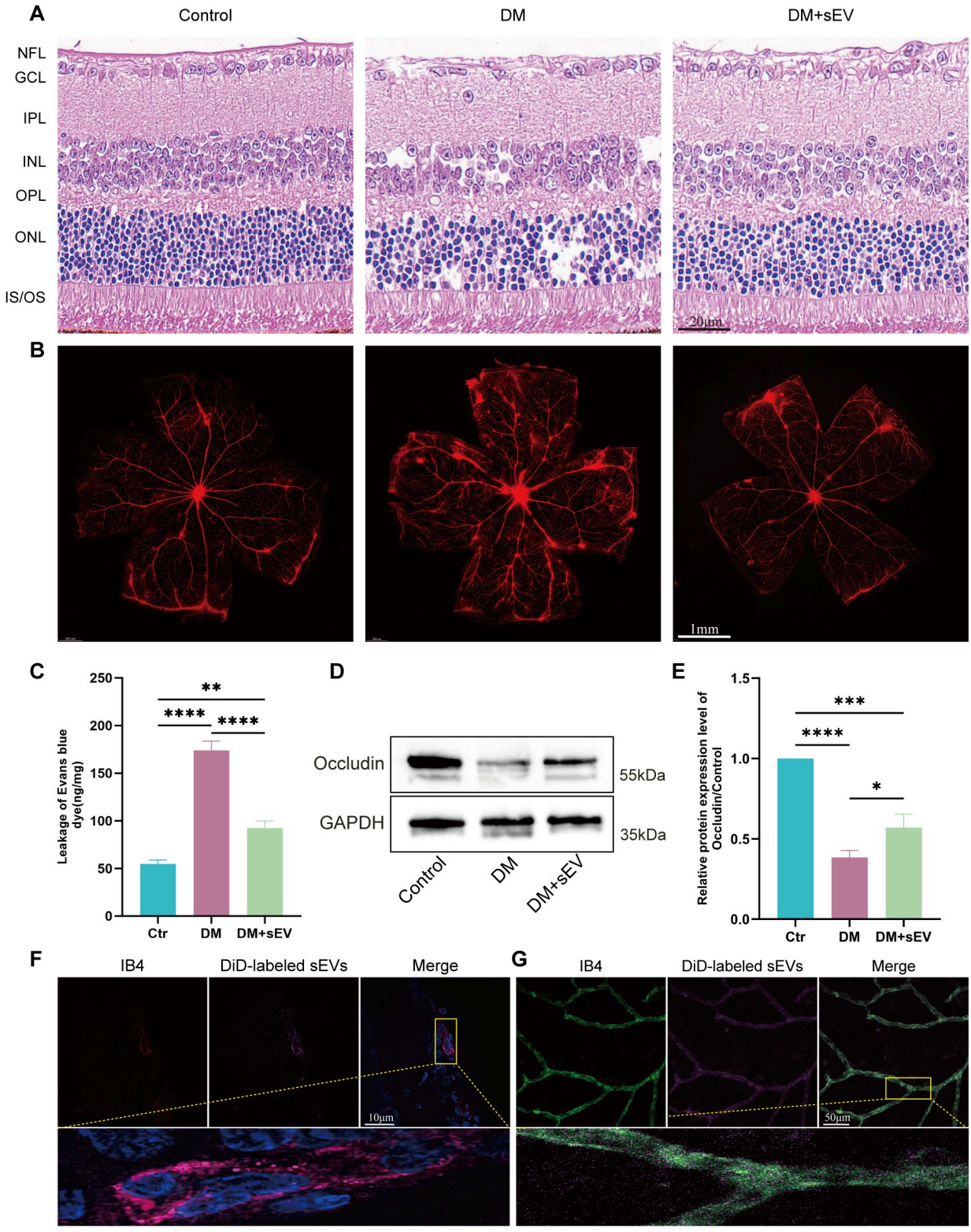

Figure 2

hiPSC-sEVs attenuate diabetic retinal injury and exhibit retinal vascular-associated fluorescence.

(A) Representative H&E-stained retinal sections from Control, DM, and DM + sEV mice. Scale bar = 20 μm. (B) Representative Evans Blue fluorescence images of retinal flat mounts. Scale bar = 1 mm. (C) Extracted Evans Blue content normalized to retinal wet weight and expressed as ng/mg; n = 3

independent mice per group, with one left retina collected from each animal. (D, E) Representative Western blots of retinal occludin and the corresponding densitometric analyses. Target signals were normalized to GAPDH and then to the control sample on the same membrane; n = 3 independent mice per group. (F, G) Representative retinal sections (F) and flat mounts (G), including enlarged views, from normal mice examined 14 days after intravitreal administration of DiD-labeled preparations; three mice were examined. Boxes indicate the regions shown at higher magnification. In (F), IB4 is red, DiD is magenta, and nuclei are blue. In (G), IB4 is green and DiD is red. Overview scale bars = 10 μm in (F) and 50 μm in (G). Quantitative data are presented as mean ± SD. Statistical analysis was performed using one-way ANOVA with Tukey's test. **P < 0.01, ***P < 0.001, ****P < 0.0001, or *P < 0.05, as indicated. DM, diabetes mellitus; NFL, nerve fiber layer; GCL, ganglion cell layer; IPL, inner plexiform layer; INL, inner nuclear layer; OPL, outer plexiform layer; ONL, outer nuclear layer; IS/OS, photoreceptor inner/outer segments.

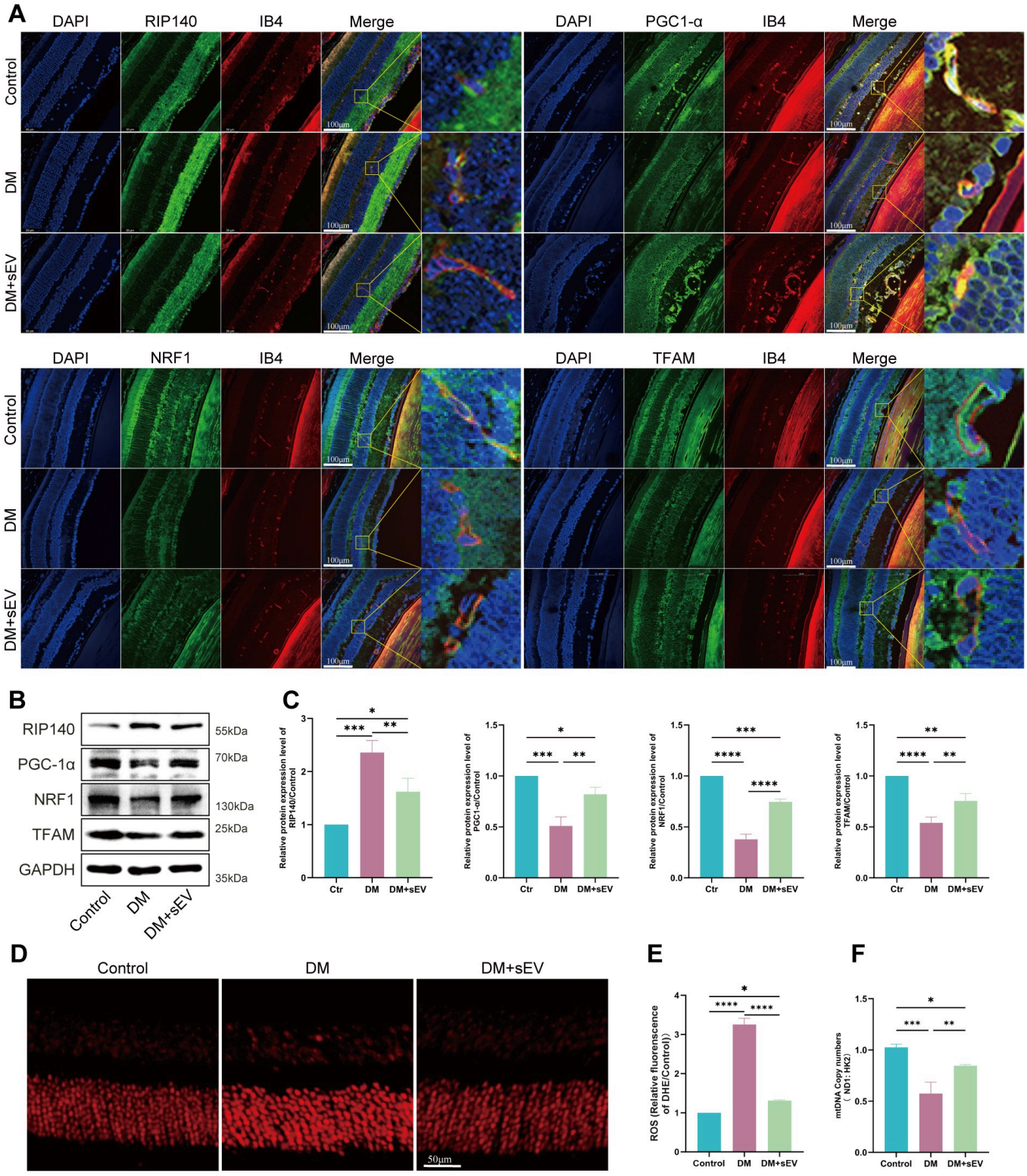

Figure 3

hiPSC-sEV treatment improves retinal mitochondrial markers and reduces oxidative stress.

(A) Representative immunofluorescence images and enlarged views showing RIP140, PGC-1α, NRF1, and TFAM alongside IB4 in retinal sections from Control, DM, and DM + sEV mice. Target proteins are shown in green, IB4 in red, and DAPI-stained nuclei in blue. Yellow boxes indicate the regions shown at

higher magnification. Overview scale bars = 100 μm. (B, C) Representative Western blots and densitometric analyses of retinal RIP140, PGC-1α, NRF1, and TFAM. Protein signals were normalized to GAPDH and expressed relative to the control sample on the same membrane. (D, E) Retinal DHE staining and quantification of relative red fluorescence intensity. Scale bar = 50 μm. (F) Relative retinal mtDNA copy number measured using Nd1 as the mitochondrial target and Hk2 as the nuclear DNA reference, expressed relative to Control. Quantitative data are presented as mean ± SD from three independent mice per group. Statistical analysis was performed using one-way ANOVA with Tukey's test. *P < 0.05, **P < 0.01, ***P < 0.001, ****P < 0.0001.

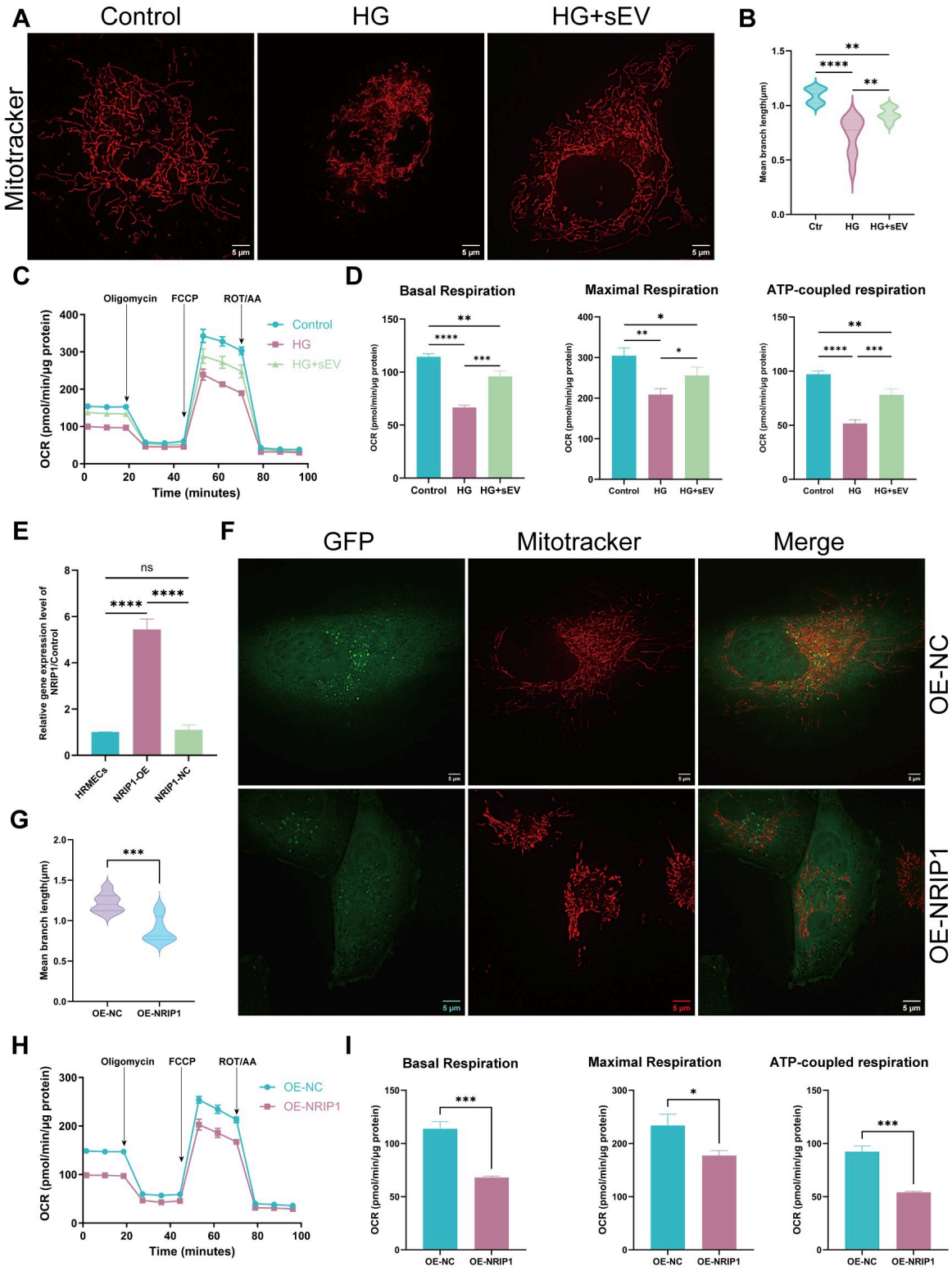

Figure 4

hiPSC-sEVs improve mitochondrial function following HG exposure, whereas NRIP1 overexpression impairs mitochondrial function under normal conditions.

(A, B) Representative live-cell MitoTracker images and quantification of mean mitochondrial branch length in Control, HG, and HG + sEV hRMECs. Following 48 h of HG exposure, cells received sEVs for 24

h while HG exposure continued. Scale bars = 5 μm. (C, D) Oxygen consumption profiles and calculated basal, maximal, and ATP-coupled respiration during the mitochondrial stress test. Oligomycin, FCCP, and rotenone/antimycin A (ROT/AA) were injected sequentially. OCR was normalized to total protein. (E) Relative NRIP1 mRNA levels in untransduced hRMECs, NRIP1-overexpressing cells, and negative-control-transduced cells, normalized to GAPDHand expressed relative to untransduced cells. (F, G) Representative GFP, MitoTracker, and merged images, together with quantification of mitochondrial branch length, in OE-NC and OE-NRIP1 cells under normal culture conditions. GFP is green, and MitoTracker is red. Scale bars = 5 μm. (H, I) OCR profiles and respiratory parameters in the same overexpression groups under normal culture conditions. Three independent experiments were performed, with eight cells per group sampled in each experiment for morphological analysis. Violin plots show cell-level distributions, whereas bar plots and time-course data are presented as mean ± SD. Statistical comparisons were performed using one-way ANOVA with Tukey's test or an unpaired Student's t-test for two-group comparisons. *P < 0.05, **P < 0.01, ***P < 0.001, ****P < 0.0001; ns, not significant.

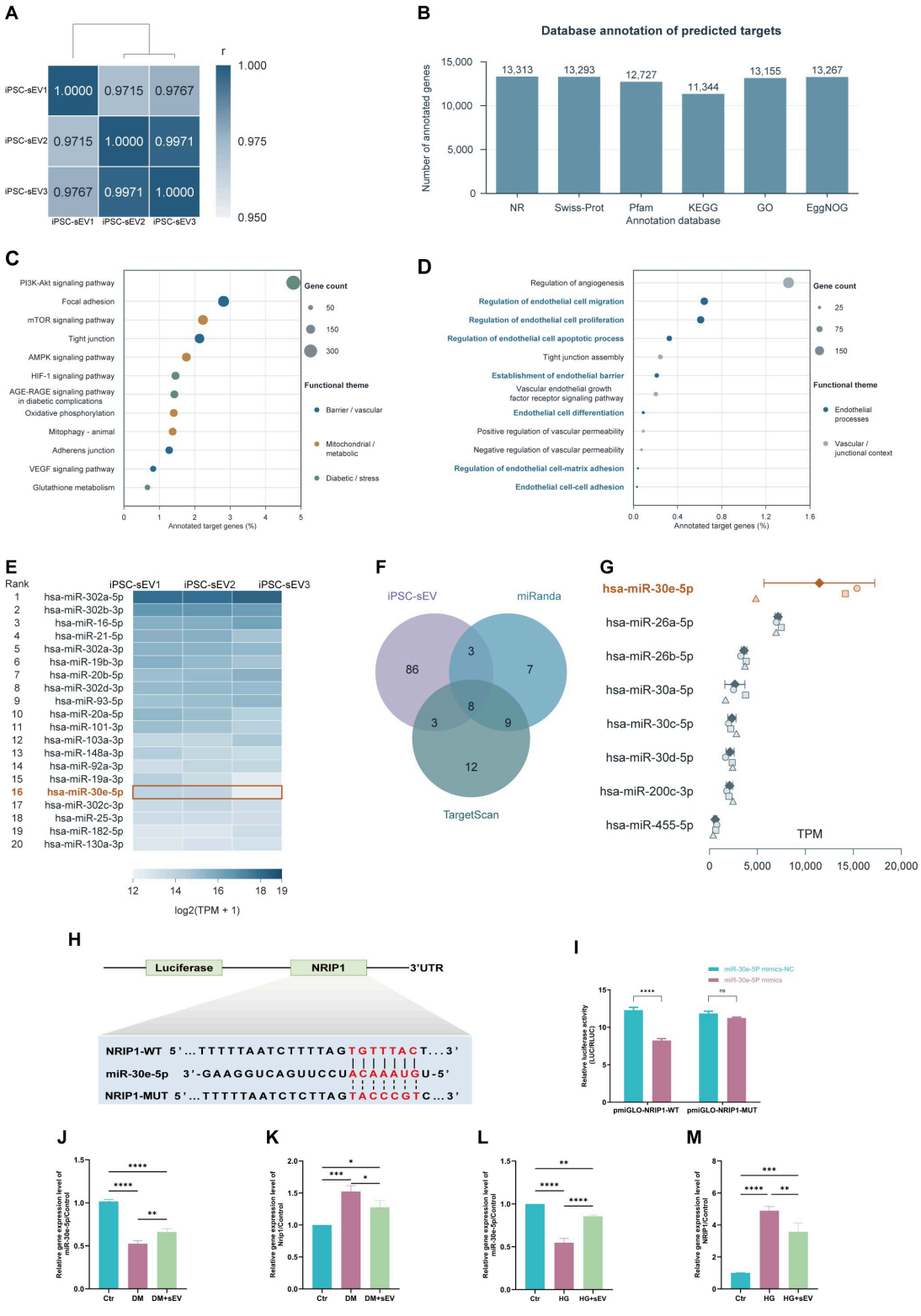

Figure 5

hiPSC-sEV miRNA profiling and validation of miR-30e-5p–NRIP1 regulation.

(A) Pearson correlation heatmap of untransformed TPM values across 1,015 detected miRNA entries from three independent hiPSC-sEV samples. Samples were clustered using average linkage and a distance metric of 1 − Pearson's r. (B) Database annotation coverage in the original project analysis. Bars

indicate the number of genes annotated in NR, Swiss-Prot, Pfam, KEGG, GO, and EggNOG, with counts shown above the bars. Genes may be annotated in multiple databases; therefore, these counts are not additive.(C, D) Theme-selected KEGG annotations (C) and GO biological process annotations (D) of predicted targets of all detected hiPSC-sEV miRNAs. (E) Heatmap of the 20 miRNAs with the highest mean TPM across three independent hiPSC-sEV samples. Colours represent log2(TPM + 1), without row-wise standardisation. These miRNAs accounted for 81.98% of the total mean TPM. miR-30e-5p, ranked 16th, is highlighted in orange. (F) Intersection of the Top100 miRNA set with ENCORI-derived miRanda and TargetScan lists of miRNAs predicted to target NRIP1, identifying eight candidates. (G) Abundance of the eight candidate miRNAs, ordered by descending mean TPM. Diamonds and horizontal whiskers indicate mean ± SD across three independent hiPSC-sEV samples. Circles, squares, and triangles identify individual samples, with their vertical positions offset for readability. miR-30e-5p is highlighted in orange. (H) Predicted miR-30e-5p-binding sequence in the NRIP1 3'UTR and the corresponding mutant sequence. (I) Relative luciferase activity in 293T cells cotransfected with the wild-type or mutant reporter and either the miR-30e-5p mimic or the mimic negative control. (J, K) Relative retinal miR-30e-5p abundance (J) and mRNA expression of the mouse gene Nrip1 (K). (L, M) Relative miR-30e-5p abundance (L) and NRIP1 mRNA expression (M) in hRMECs. U6 and GAPDHwere used as the respective reference targets for miRNA and mRNA measurements. Data in (I–M) are presented as mean ± SD, with n = 3 per group. Retinal measurements were obtained from independent mice, and cell-based assays were performed in independent experiments. Two-group comparisons were analyzed using two-sided unpaired Student’s t-tests, and multiple-group comparisons were analyzed using one-way ANOVA followed by Tukey’s multiple-comparison test. Brackets indicate the groups compared. *P < 0.05, **P < 0.01, ***P < 0.001, ****P < 0.0001; ns, not significant. TPM, transcripts per million; WT, wild type; MUT, mutant.

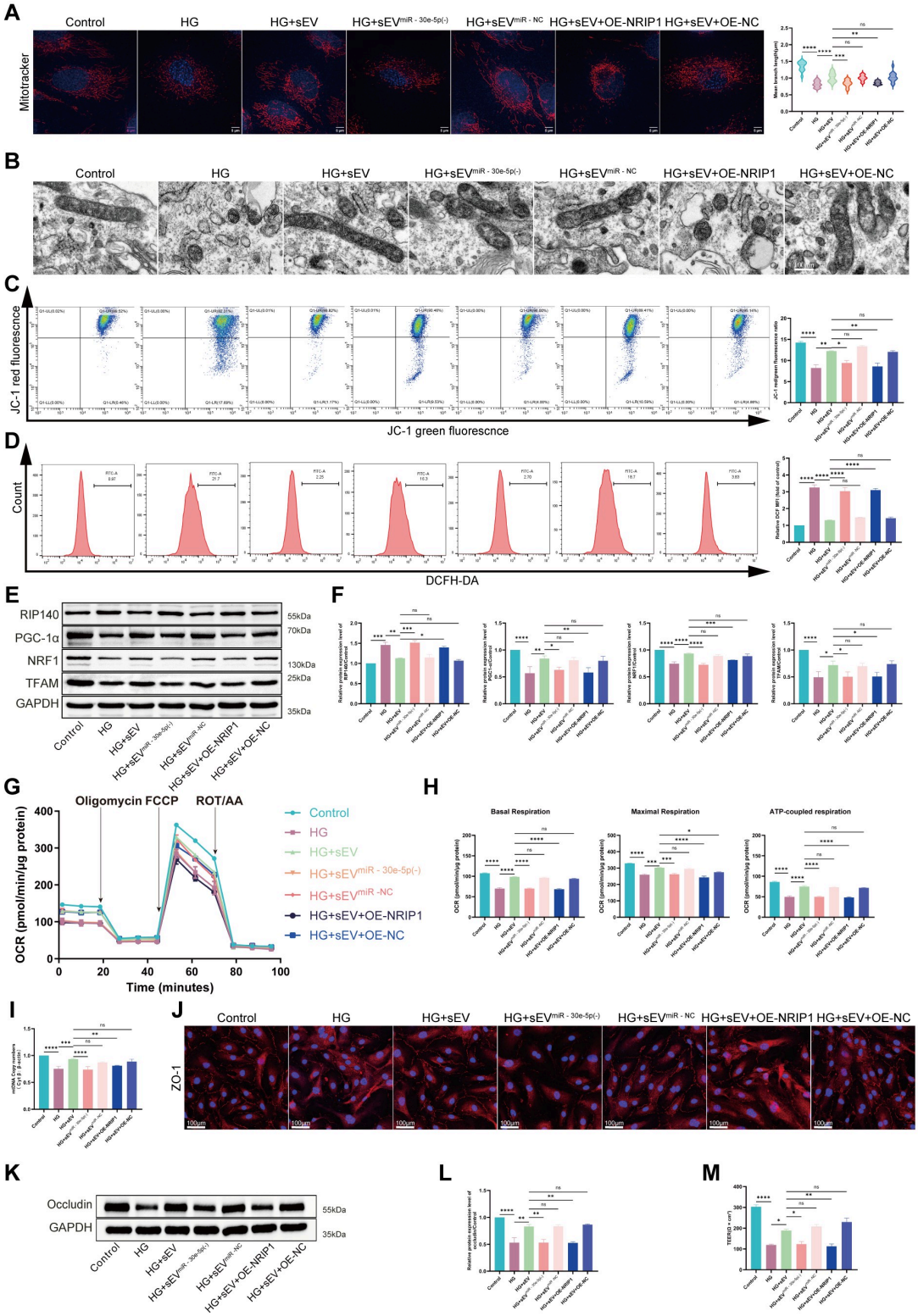

Figure 6

miR-30e-5p-associated mitochondrial and endothelial barrier responses to hiPSC-sEV treatment.

hRMECs were assigned to the Control, HG, HG + sEV, HG + sEV-miR-30e-5p-KD, HG + sEV-miR-NC, HG + sEV + OE-NRIP1, and HG + sEV + OE-NC groups. sEV-miR-30e-5p-KD denotes preparations isolated after hiPSCs were transduced with a miR-30e-5p knockdown lentiviral vector; sEV-miR-NC denotes

preparations from control-lentivirus-transduced hiPSCs. (A) Representative MitoTracker images and mean mitochondrial branch length. Scale bars = 5 μm. Violin plots display cell-level distributions across three independent experiments. (B) Representative mitochondrial transmission electron micrographs. Scale bar = 100 nm. (C) JC-1 flow cytometry results and red/green fluorescence ratios. (D) DCFH-DA flow cytometry results and mean DCF fluorescence relative to Control. (E, F) Western blots and densitometric analyses of RIP140, PGC-1α, NRF1, and TFAM, normalised to GAPDH and expressed relative to Control. (G, H) OCR profiles and basal, maximal, and ATP-coupled respiration following sequential addition of oligomycin, FCCP, and rotenone/antimycin A; OCR was normalised to total protein. (I) Relative mtDNA copy number measured using CytBand ACTBas mitochondrial and nuclear DNA targets, respectively. (J) Representative ZO-1 staining in red, with DAPI-stained nuclei in blue. Scale bars = 100 μm. (K, L) Western blots of occludin and corresponding densitometric analyses, normalised to GAPDH and expressed relative to Control. (M) TEER of hRMEC monolayers. Cell-free insert resistance was subtracted, and the corrected resistance was multiplied by the membrane area to yield values in Ω·cm2.

Quantitative assays, including TEER, were performed in three independent experiments. Bar and OCR data are presented as mean ± SD. Comparisons were performed using one-way ANOVA followed by Tukey's multiple-comparison test. Each bracket identifies the two groups being compared; symbols do not indicate a common reference group unless it is an endpoint of the corresponding bracket. In (M), HG + sEV is compared with HG and separately with the KD, miR-NC, OE-NRIP1, and OE-NC groups. TEM and ZO-1 images were assessed qualitatively. *P < 0.05, **P < 0.01, ***P < 0.001, ****P < 0.0001; ns, not significant.

Supplementary Files

This is a list of supplementary files associated with this preprint. Click to download.

- SupplementaryInformationOriginalWesternBlots.pdf